Time-of-flight neutron interferometry

H. Rauch and H. Wölwitsch*
Atominstitut der Österreichischen Universitäten, A-1020 Wien, Austria

R. Clothier,† H. Kaiser, and S. A. Werner
Physics Department, University of Missouri–Columbia, Columbia, Missouri 65211
and Research Reactor Facility, University of Missouri–Columbia, Columbia, Missouri 65211
(Received 22 July 1991; revised manuscript received 12 December 1991)

In the experiment described in this paper, a chopper serves as a source of neutron intensity pulses which pass through a perfect Si-crystal neutron interferometer (NI), where they are split coherently into two parts that recombine and interfere. As the occupation number of a single pulse is much smaller than unity, the results very clearly demonstrate the single-particle interference phenomena of neutron interferometry experiments. While traveling the pulses spread, with faster (slower) neutrons tending toward the leading (trailing) edge. The coherence length of the neutrons depends on the spectral width of their wavelength distribution. When a material with a neutron-nuclear optical potential is placed in one beam path in the NI, there is a loss of fringe visibility (contrast), which depends on the coherence length. By using time-of-flight techniques, we divide the pulse into time segments. Within a given time slice, the wavelength spectrum is narrower than in the pulse as a whole. As a result, contrast remains in the time slices even when it disappears in the overall pulse. We also observe an additional contrast modulation due to the overlap of neighboring pulses.

PACS number(s): 03.65.Bz, 07.60.Ly

I. INTRODUCTION

Most neutron interferometer experiments performed until now have dealt with stationary situations where the phenomena are completely described by the stationary Schrödinger equation (e.g., [1–3]). Time-dependent effects appear if a time-dependent Hamiltonian or time-dependent boundary conditions act on the system. In this case the phenomena are described by the time-dependent Schrödinger equation

$$H\psi(\mathbf{r},t)=i\hbar\frac{\partial\psi(\mathbf{r},t)}{\partial t}\ , \tag{1}$$

which adds the time parameter and permits energy exchange between the quantum system and the measuring apparatus. Although the experiments being described belong to the quasistationary regime where the energy change is small, the observed phenomena will show distinct correlation between the interference pattern and the time structure of a pulsed beam behind a fast chopper system.

The observed interference phenomena are described by the coherence function $\Gamma(\mathbf{\Delta},t)$ which is given by the autocorrelation function of the overlapping wave functions

$$\Gamma(\mathbf{\Delta},t)=\langle\psi^*(0,0)\psi(\mathbf{\Delta},t)\rangle\ , \tag{2}$$

where $\mathbf{\Delta}=\mathbf{r}'-\mathbf{r}''$ and $t=t'-t''$ are the spatial and temporal shifts of these wave functions (e.g., [4]). $\Gamma(\mathbf{\Delta},0)$ and $\Gamma(0,t)$ denote the spatial and temporal coherence functions, respectively.

The interference pattern of a perfect crystal interferometer is governed by the phase shift between the two overlapping beams which gives in the case of an ideal arrangement

$$I\propto|\psi_r+\psi_l|^2=|\psi|^2|1+e^{i\chi}|^2\propto(1+\cos\chi)\ , \tag{3}$$

where the phase shift χ is given by the path integral of the canonical momentum along the beam paths. In the case of a homogeneous phase shifter of thickness D_0, with a surface normal $\hat{\mathbf{n}}$ and with an index of refraction $n=1-\lambda^2Nb_c/2\pi$ (λ is the neutron wavelength, N the particle density, and b_c the coherent scattering length) one gets

$$\chi=\oint\mathbf{k}\cdot d\mathbf{s}=(1-n)kD_{\rm eff}=\Delta kD_{\rm eff}\ , \tag{4}$$

with $D_{\rm eff}=D_0/(\hat{\mathbf{k}}\cdot\hat{\mathbf{n}})$. According to Snell's law, only the normal $\mathbf{k}$ component changes and the momentum vectors inside ($\mathbf{K}$) and outside ($\mathbf{k}$) the sample can be written as [5]

$$\mathbf{K}-\mathbf{k}=(1-n)k\hat{\mathbf{n}}/(\hat{\mathbf{k}}\cdot\hat{\mathbf{n}})\ , \tag{5}$$

which permits the definition of the spatial shift of the wave trains

$$\mathbf{\Delta}=\frac{(\mathbf{K}-\mathbf{k})}{k}D_0\ . \tag{6}$$

Thus one can reformulate the phase factor in the form

$$e^{i\chi}=e^{i\mathbf{\Delta}\cdot\mathbf{k}}\ . \tag{7}$$

A wave-packet description has to be used to account for the finite momentum width of the beams. This causes the coherence function to become

$$\langle|\Gamma(\Delta)|\rangle=(2\pi)^{-3/2}\int\rho(\mathbf{k})e^{i\mathbf{k}\cdot\Delta}d\mathbf{k}\ , \tag{8}$$

which can be interpreted as the Fourier transform of the momentum distribution function $\rho(\mathbf{k})$ or as an average over the phase factor as defined in Eq. (7). In the case of normal distributions one can use the relation (e.g., [6])

$$\langle e^{i\chi}\rangle=e^{i\chi}\exp(\langle\delta\chi^2\rangle/2)\ , \tag{9}$$

which yields for Gaussian momentum distributions with widths δk_i an intensity modulation

$$I\propto(1+\langle|\Gamma(\Delta)|\rangle\cos\chi)\ , \tag{10}$$

with

$$\langle|\Gamma(\Delta)|\rangle=\prod_{i=x,y,z}\exp[-(\Delta_i\delta k_i)^2/2]\ . \tag{11}$$

One notices that in a perfect crystal interferometer the damping factor depends strongly on the orientation of the phase shifter because $\delta\mathbf{k}$ is very small along the reflecting lattice vector of the reflecting planes. Related experiments have been reported in the literature to elucidate the quantum-mechanical coherence properties of matter waves [7–12]. From the reduction of the coherence function at large phase shifts the related coherence length has been deduced $[\Delta x_i^c=(2\delta k_i)^{-1}]$. δk_i can be defined before or behind the interferometer as we will see from the following results. Phase variations due to variations of the sample thickness δD can be treated similarly by adding a factor $\exp[-(2\pi\delta D/D_\lambda)^2/2]$ where D_λ denotes the λ thickness of the sample $[D_\lambda=2\pi/(Nb_c\lambda)]$. Absorption and other loss processes have to be described by an imaginary term to the index of refraction and a factor $\exp[-\sigma_r ND/2]$ is added, where σ_r is a so-called removal cross section accounting for absorption, scattering, and diffraction effects if they remove particles from the original phase space volume defined above [13,14]. The related momentum resolutions (δk_i) can be defined as before, inside or behind the interferometer. Thus, in cases where the overall momentum width prevents the observation of an interference pattern behind the interferometer [Eq. (11)], spectral filtering behind the interferometer due to an additional crystal reflection [11], or a time-of-flight analysis as done in [15,16] and in this work, can recover the interference pattern. In another experiment, the interference pattern of simultaneously diffracted first- and second-order neutrons have been observed by using a time-resolved measuring technique at a pulsed source [17].

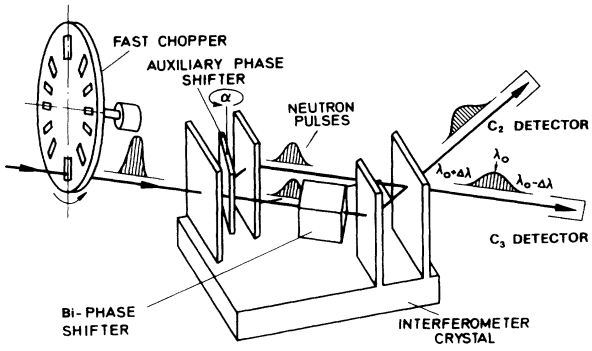

FIG. 1. Sketch of the experimental setup for pulsed neutron interferometry measurements.

In the following sections we will describe experiments which demonstrate how the interference pattern changes in time-resolved measurements where the momentum distribution within certain time slices can be made much narrower and where frame overlap effects of faster and slower neutrons from neighboring pulses can be observed. The main components of the experimental setup are shown in Fig. 1.

II. TIME-DEPENDENT EFFECTS

The motion of a free wave packet is described by the time-dependent Schrödinger equation (1). In the case of minimum uncertainty packets with Gaussian widths δx and δk in real and momentum space $(\delta x\delta k=\frac{1}{2})$ one expects the quantum-mechanical spreading as a function of time (e.g., [18])

$$[\delta x(t)]^2=[\delta x(0)]^2+\left[\frac{(\hbar/2m)t}{\delta x(0)}\right]^2\ . \tag{12}$$

This minimum uncertainty wave packet is difficult to achieve because $\delta x(0)$ has to approach the coherence length $\Delta x^c\sim(2\delta k)^{-1}$ as discussed previously. This also means that pulse lengths of the order of the coherence time $\Delta t^c=\Delta x^c/v$ have to be produced which means chopper opening times of the order of ns. In this case, diffraction in time would play an important role which is completely analogous to the well-known single slit diffraction phenomena in real space [19–21]. Thus, Fraunhofer- and Fresnel-like phenomena are expected to occur which change the energy of the beam accordingly. For a triangular slit opening for a time Δt one expects for an incident plane wave with a frequency ω_0 a frequency spectrum

$$|\phi(\omega)|^2\propto\left[\frac{\sin(\omega-\omega_0)\Delta t}{\omega-\omega_0}\right]^2\ . \tag{13}$$

For long opening times $(\Delta t\gg\Delta t^c)$ diffraction effects occur at the edges only which can be neglected in most cases. Then the phenomena can be described by classical distribution functions and their spreading happens similarly in the quantum case. For Guassian pulses one gets

$$[\delta x(t)]^2=[\delta x(0)]^2+[\delta v\,t]^2 \tag{14}$$

where one notices the similarity to Eq. (12) if one uses the de Broglie relation and $\Delta x^c=(2\delta k)^{-1}=\lambda^2/4\pi\delta\lambda$. In terms of the temporal pulse length one obtains

$$[\Delta t]^2=[\Delta t_p]^2+\left[\frac{\delta\lambda}{\lambda}t_0\right]^2\ , \tag{15}$$

where Δt_p is the opening time of the chopper and $t_0=L/v_0$ is the average time of flight of neutrons between the chopper and the detector at distance L. In fact, Eq. (15) which describes the broadening of the intensity pulse is identical to the expression which describes

the broadening of a quantum-mechanical wave packet [Eq. (12)] except for the fact that in Eq. (15) $\delta x(0)=v\,\delta t_p$ does not fulfill the minimum uncertainty relation. The mean wavelength of neutrons being measured at time t at a detector with an effective thickness Δd becomes in the classical limit [$\delta x(0)\gg\Delta x^c$]

$$\langle\lambda(t)\rangle=\lambda_0[1+t_0(t-t_0)(\delta\lambda/\lambda_0)^2/(\Delta t')^2]\ , \tag{16}$$

with

$$[\Delta t']^2=[\Delta t]^2+[\Delta d/v_0]^2\ .$$

Due to $\langle\chi(t)\rangle\propto\langle\lambda(t)\rangle$ we get a similar equation for the phase shift

$$\langle\chi(t)\rangle=\chi_0[1+t_0(t-t_0)(\delta\lambda/\lambda_0)^2/(\Delta t')^2]\ . \tag{17}$$

Related measurements using a similar setup at the high flux reactor at Grenoble were given previously [14,15].

At a position L at a time t there still exists in a certain time channel a Gaussian distribution with a restricted spectral width given by

$$\left[\frac{\delta\lambda}{\lambda_0}\right]'^2=\left[\left[\frac{\lambda_0}{\delta\lambda}\right]^2+\left[\frac{t_0}{\Delta t'}\right]^2\right]^{-1}\ , \tag{18}$$

which causes less diminution of the interference contrast for measurements with narrow time channels than for the whole beam [Eq. (11), notice $\delta\lambda/\lambda_0=\delta k/k_0$].

We now know how neutron pulses spread as they propagate. At larger distances downstream the edges of each pulse begin to overlap incoherently with the preceding and following ones. Gaussian-shaped neutron pulses produced within a time interval T, corresponding to wavelength $\lambda_1=\lambda_0-\delta\lambda$ and $\lambda_2=\lambda_0+\delta\lambda$, overlap at a distance $L^c=hT/2m\delta\lambda$ downstream from the chopper. The spectral width at the relevant time interval is given by the spectral widths around λ_1 and λ_2. The measured intensity in the related time slice around $t=t_0^c(1-\delta\lambda/\lambda_0)$ is given as [15,21]

$$\begin{aligned}I(\lambda_1,\lambda_2)&=I(\lambda_1)+I(\lambda_2)\\&\propto 2+\langle|\Gamma(\Delta_1)|\rangle\cos\chi_1+\langle|\Gamma(\Delta_2)|\rangle\cos\chi_2\ .\end{aligned} \tag{19}$$

In the case of material phase shifters arranged perpendicularly to the beam (Fig. 1) and for rather narrow Gaussian wavelength distributions around λ_1 and λ_2 [Eq. (18)] one can reformulate this equation to be

$$\begin{aligned}I(\lambda_1,\lambda_2)\propto\{1+\exp[-\chi_0^2(\delta\lambda/\lambda_0)^2/2]\\\times\cos(Nb_cD\Delta\lambda)\cos(Nb_cD\bar{\lambda})\}\ ,\end{aligned} \tag{20}$$

where we have used

$$\langle|\Gamma(\Delta_1)|\rangle\approx\langle|\Gamma(\Delta_2)|\rangle-\exp[-(\Delta\delta k)^2/2]\ , \tag{21}$$

and the definitions

$$\bar{\lambda}\equiv(\lambda_1+\lambda_2)/2,\quad \Delta\lambda\equiv(\lambda_1-\lambda_2)/2\ , \tag{22}$$

and

$$\chi_0\equiv -Nb_cD\lambda_0\ . \tag{23}$$

Thus, the total intensity exhibits a series of "beats," modified by a decaying exponential. The contrast of the intensity pattern as a function of the thickness of the phase shifter is given by

$$\begin{aligned}C(D)&=\frac{I_{\max}-I_{\min}}{I_{\max}+I_{\min}}\\&=|\cos(Nb_cD\Delta\lambda|\exp[-\chi_0^2(\delta\lambda/\lambda_0)^2/2]\ .\end{aligned} \tag{24}$$

The exponential term is due to the wavelength spread and the cosine term represents a contrast oscillation caused by the overlap of two pulses, i.e., the contrast is expected to vary according to a damped cosine function going through a series of minima and maxima.

III. EXPERIMENT

A fast mechanical neutron chopper was added to the neutron interferometer setup at beam port C at the University of Missouri Research Reactor (MURR) as shown in Fig. 1. The chopper was built by URANIT in Germany and consists of a 17.0-cm-diam aluminum disk, mounted on the end of a magnetized steel shaft, and enclosed in an evacuated, electronically controlled drive mechanism. The shift is suspended and set in motion by rotating magnetic fields, up to a frequency of $\sim$45 500 rpm. The vacuum in the vessel is maintained at $\sim10^{-5}$ Torr to reduce friction. There are 60 grooves milled around the outer edge of the disk, each 6 mm wide $\times$15 mm high, separated from each other by 1.5-mm gaps, and filled with a Gd_2O_3-epoxy mixture. Since Gd absorbs thermal neutrons, the 1.5-mm-wide Al gaps between the Gd_2O_3 regions act as neutron slits, opening and closing 60 times per revolution. The Gd and Al regions were made with a size ratio of 4:1, so that the chopper is closed 80% of the time (Fig. 2). A Cd slit, 1.5×15 mm^2, was affixed to the cover of the drive mechanism, directly downstream from the chopper disk. The combination of stationary and rotating slits creates a train of triangular intensity pulses which can be approximated by Gaussian shapes. At maximum speed, the chopper produces pulses in an interval of $T=22$ μs and 4.40 μs in duration [full

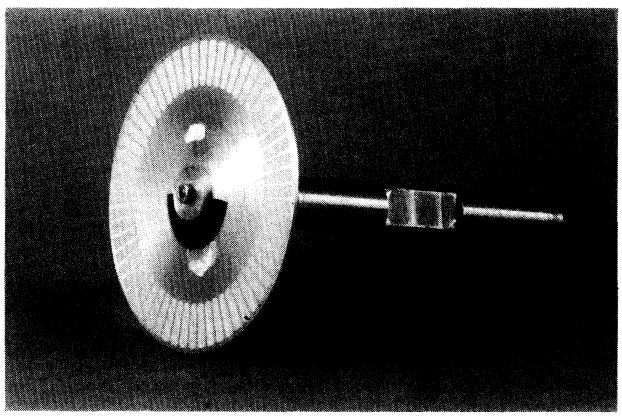

FIG. 2. Photograph of the neutron chopper disk showing also the magnetized shaft for the magnetic bearing.

width at half maximum (FWHM)] which corresponds to a standard width $\Delta t_p = 1.869$ μs (Fig. 3).

It should be noted that these intensity pulses are actually probability distributions. The number of neutrons contained within each pulse depends on the intensity of the incident beam. In the experiment, the neutron intensity was so low that most (99.995%) of the "pulses" were in fact empty. After summing many of these "pulses," however, the neutrons are distributed according to the expected pulse-shaped probability distribution. Also, despite the similarities, an intensity pulse is not the wave packet of an individual neutron. In the wave-packet picture, the physical extent of the neutron is given by its coherence length (Δx_i^c), which for this experiment was $\Delta x^c \approx 160$ Å. The spatial length of the neutron intensity pulse, on the other hand, is determined solely by how long the slit remains open, and was at least 7 mm in this experiment. Thus, an intensity pulse may contain within it many (or perhaps no) individual (much smaller) neutron wave packets. We shall see, however, that the propagation and spreading of the pulse is theoretically very similar to that of a wave packet [Eqs. (12) and (14)].

The beam incident on the interferometer is produced by reflection off the (002) planes of a pyrolytic graphite monochromator. At a take-off angle of 41°, this produces a beam of nominal wave length $\lambda_0 = 2.349$ Å and spectral width $\delta\lambda/\lambda = 0.005\,05$. The beam then passes through a 5-cm cube of pyrolytic graphite, which filters out the $\lambda = 1.17$ Å neutrons. The chopper then chops the beam into intensity pulses, which subsequently pass through a 8×6 mm^2 slit and then strike the neutron interferometer (NI). The pulses spread as they propagate, as discussed in Sec. II. The perfect silicon NI uses the (220) lattice planes at a Bragg angle $\theta_B = 37.71°$. Some of the neutrons are diffracted by the NI and enter one of the exit beams, C2 or C3. If allowed to travel far enough downstream, the spreading pulses will eventually overlap with adjacent pulses, before entering one of the ^{3}He detectors. A summary of the symbols and their experimental values for the setup used is given in Table I.

To provide thermal and vibrational stability, the NI is housed inside an aluminum enclosure, which is mounted

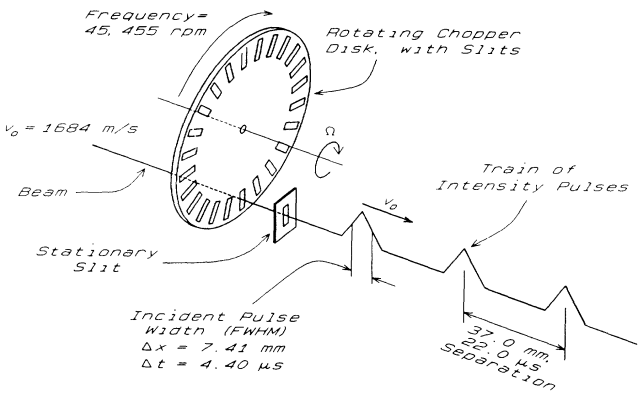

FIG. 3. A train of neutron pulses, created by passing a beam through the rotating chopper disk in front of a stationary slit.

on a granite table and enclosed within a large masonite box. The granite table is supported by four vibration-isolation pneumatic cushions, and the entire apparatus is enclosed by a large plexiglass box, to provide additional environmental isolation. In this experiment, the C2 detector was mounted vertically inside the aluminum box, and was not used in a significant way. The C3 "detector" actually consisted of four horizontal 20-atm ^{3}He proportional detectors, each a cylinder with a 1.27 cm diameter, stacked one above the other, and all feeding into the same electronic detection channel. They contribute to the time uncertainty by $\Delta t_D = \Delta d / v_0 = 1.36$ μs. The C3 detectors were mounted as far downstream as physically possible: 277 cm from the chopper inside a masonite shielding drum. At that distance the pulse length at the highest repetition rate used was $\Delta t' = 8.62$ μs [Eqs. (15) and (16)]. The masonite drum was lined with 5 cm of B_4C powder, which reduced the C3 neutron background to 9.4 counts/min. This was necessary, because the chopped C3 beam at this position had an average intensity of only 28.4 counts/min.

The output from the detectors fed into a time-of-flight data collection system. The data were collected in 1-μs time bins. Once per revolution, every 1320 μs, a signal

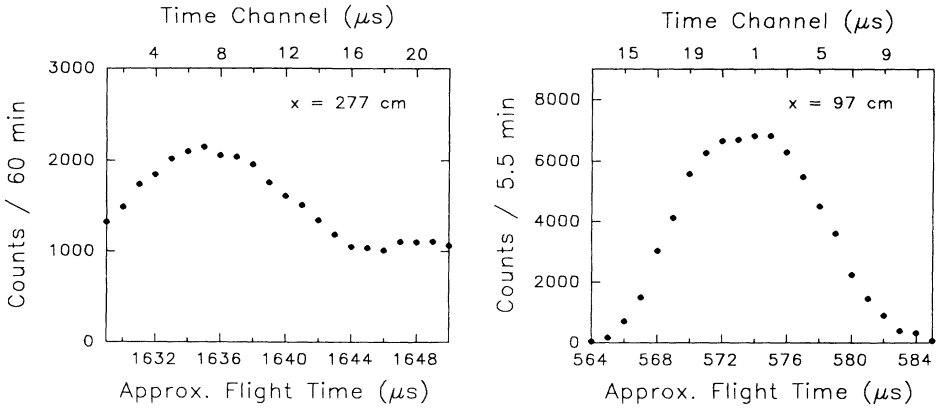

FIG. 4. The pulse shape $I(t)$ in the C3 exit beam, measured at a distance of 97 and 277 cm from the chopper. The background has been subtracted.

from the chopper disk was used to synchronize the system. During one revolution, 60 pulses were produced in 22-μs intervals. After accumulating data over many revolutions, the 60-pulse pattern was summed into one 22-μs window. Figure 4 shows pulse shapes measured in this way at a distance $x=97$ cm from the chopper and at $x=277$ cm where most experiments have been performed. At $x=97$ cm, the pulses are still isolated, but at $x=277$ cm, they have spread enough so that neighboring pulses overlap as is shown schematically in Fig. 5.

With this arrangement, we were able to carry out NI experiments using only those neutrons that arrived within a certain time slice of the pulse. The experimental strategy was the following: We placed a sample of thickness D in beam II in the NI, and did a series of 33 measurements of the intensity $I(D,\alpha,t)$, each corresponding to a different angular position α of the auxiliary phase shifter [α from $-0.8°$ to $+0.8°$ in steps of 0.05°, corresponding to phase steps of $\Delta\phi_p(\alpha)=25°$]. We split each pulse into 11 time slices, each 2 μs wide, and counted the

TABLE I. Definitions of symbols and their experimental values.

Symbol	Definition	Value
$C(D)$	Contrast of the interference pattern measured with a phase shifter of thickness D (C_R is relative contrast)	variable (see Table II)
D_λ	λ thickness of the sample	variable
χ	Phase shift between the coherent beams due to the Bi sample	56.5 rad/mm
$\Gamma(\Delta,t)$	First-order coherence function. $\Gamma(\Delta)$ is the spatial and $\Gamma(t)$ the temporal coherence function	variable
λ_0	Mean wavelength of the beam	2.349 Å
$\delta\lambda$	Gaussian spectral width	0.0119 Å
$\Delta d/v_0$	Time resolution of the detector with an effective thickness Δd	1.36 μs
L^c	Overlap distance of two successive pulses	3.656 m
δk_i	Gaussian momentum width of the beam in direction i	variable
$\hat{\mathbf{n}}$	Unit vector perpendicular to the sample surface	variable
t_0	Time at which the overall pulse (mean wavelength λ_0) reaches the detector at distance x	1645 μs ($x=2.77$ m)
Δt	Gaussian temporal length of the neutron pulse at distance x	8.51 μs ($x=2.77$ m) 3.45 μs ($x=0.97$ m)
Δt_p	Opening time of the chopper (Gaussian equivalent)	1.869 μs
$\Delta t'$	Gaussian temporal length of the neutron pulse at the detector, including the time resolution of the detector.	8.62 μs ($x=2.77$ m) 3.71 μs ($x=0.97$ m)
T	Time interval between successive pulses	22 μs
v_0	Mean velocity of the neutrons	1684 m/s
$\delta x(t)$	Gaussian spatial length of the neutron pulse	14.4 mm ($x=2.77$ m)
$\delta x(0)$	Gaussian spatial length of the neutron pulse behind the chopper	3.15 mm
Δx^c	(Longitudinal) coherence length of the beam	$\Delta x^c=(2\delta k)^{-1}$ = 160 Å

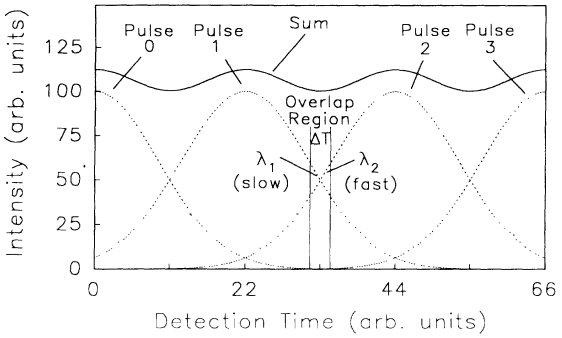

FIG. 5. Overlapping pulses in the detector vs time.

number of neutrons in each slice. When plotted versus α, this gave 11 interferograms, each corresponding to a 2-μs region of the pulse. Such a series of curves is shown in Fig. 6. The sample used for this data set was a polished bismuth slab, 12.26 mm thick. At a given auxiliary phase shifter position α_1, the sample was driven out of the beam, so that $D=0$ ("sample out"), and the contrast reduction due to coherence limitations are negligible [Eq. (11)]. During a measurement time of about 45 min, an average of 1500 neutrons were detected, and divided among the 11 time slices. The sample was then driven back into the beam ("sample in"), and the measurement was repeated with a counting time twice as long (about 90 min). The phase rotator was moved to a new position, α_2, and the process repeated; then again with α_3, α_4, and so on, resulting in the plots in Fig. 6. Note how the initial phase of the sample-in interferograms varies from slice to slice. This indicates that the mean wave length λ varies across the pulse [Eq. (16)], as previously shown in the course of a measurement at the high flux reactor at Grenoble [16]. A least-square fit (shown by the solid lines in Fig. 6) gives the contrast of each plot, and, after correcting for attenuation, the ratio of the sample-in to sample-out contrast gives the relative contrast $C_R(D)$ in each time slice (see [10]). The relative contrast $C_R(D)$ is defined as the contrast measured with a sample of thickness D divided by the contrast of the empty interferometer $[C_R(D)=C(D)/C(0)=\langle|\Gamma(\Delta)|\rangle/\langle|\Gamma(0)|\rangle]$, where $C(0)$ accounts for all experimental imperfectness of the setup [in our case $C(0)\sim 50\%$]. The relative contrast for the plots in Fig. 6 is shown in Fig. 7. Note the distinct dip in the relative contrast around time channel 7. Summing the plots in Fig. 6 (right) over all 11 time slices gives the interferogram for the overall pulse, including all neutrons. The same curve would be obtained in a steady-state experiment. Figure 8 shows the sample-out and sample-in interferograms for the overall pulse with the $D=12.26$ mm Bi sample; the absolute contrast of the curves is $(45.0\pm1.0)\%$ and $(0.4\pm0.7)\%$, respectively, giving a relative contrast of $(0.9\pm1.5)\%$. Note that the overall sample-in interferogram has almost no contrast (0.4%), although the interferograms in the time slices in Fig. 6 exhibit considerable contrast.

It took three days to complete such a "data run" for a given sample thickness, as described above and shown in Figs. 6–8. The sample was then replaced with another Bi sample of a different thickness, and another data run was taken. Bismuth has a large, positive scattering length

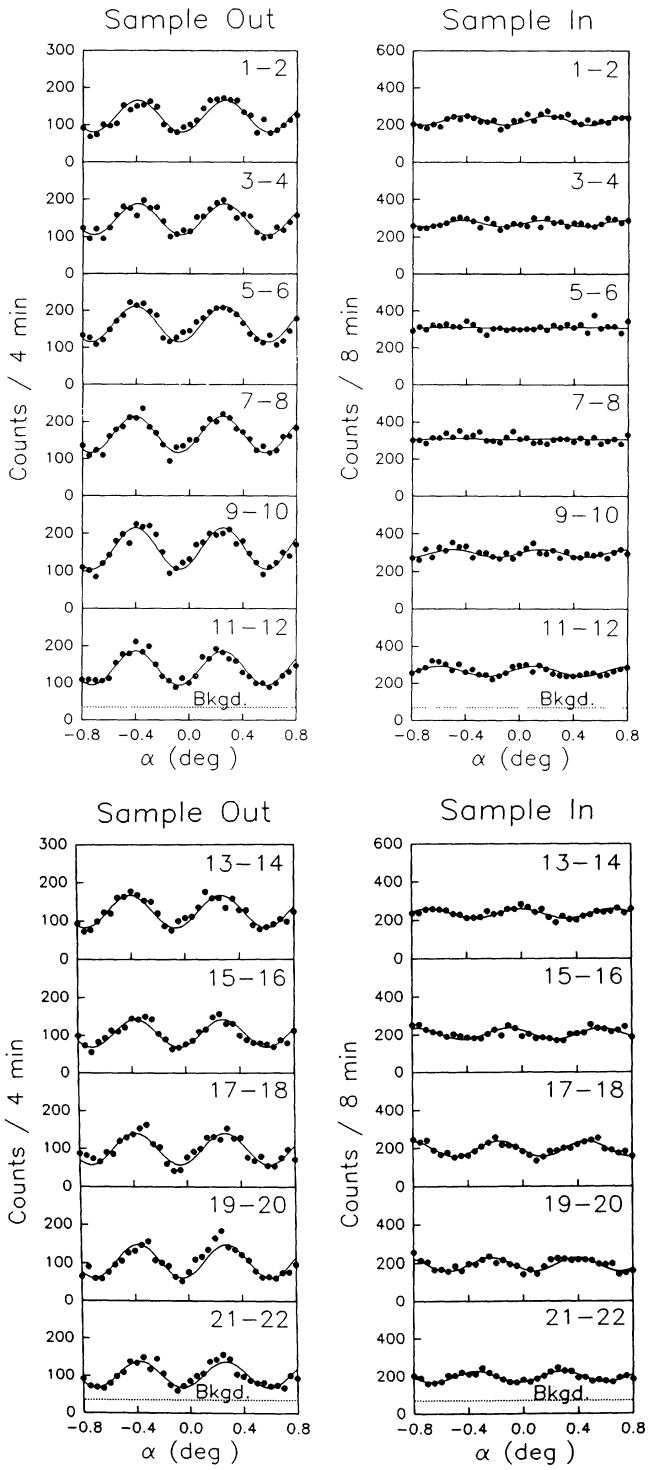

FIG. 6. Interferogram patterns in the eleven time slices, for the 12.26-mm Bi sample, for both the C3 sample-out and sample-in conditions. The numerals in the upper right of each indicate the 1-μs time channels which were combined to make up the 2-μs time slices.

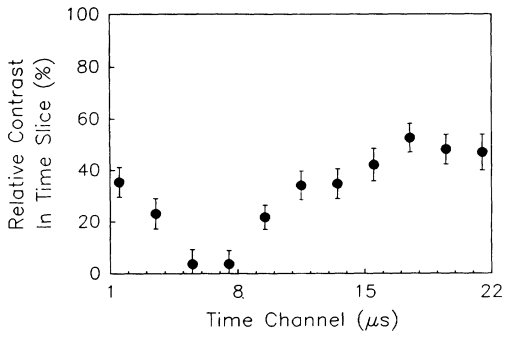

FIG. 7. The relative contrast of the C3 interferograms in the time slices, for the 12.26-mm Bi sample.

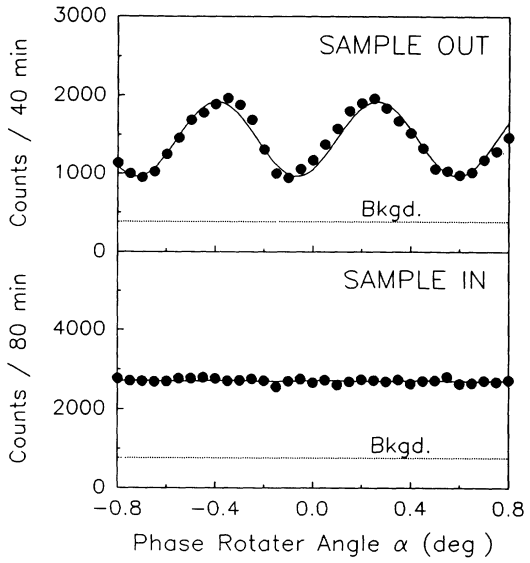

FIG. 8. C3 interferograms for the overall beam, run 73, 12.26-mm Bi, for both the sample-out and sample-in conditions.

$b=8.533$ fm, an atom density $N=2.82\times10^{28}$ m^{-3}, and relatively low absorption ($\sigma_a=0.0388$ b). Initially, four slab-shaped samples of bismuth were machined and polished, and then epoxied onto aluminum mounting brackets. The samples were made so that their nominal thicknesses were multiples of 4 mm (4, 8, 12, and 16 mm), and were numbered sequentially from 1 to 4. The exact thicknesses of the samples are given in Table II. In addition, a fifth sample was made which was thinner than the others (2.1 mm thick). Since this sample is about half as thick as sample no. 1, it was dubbed "sample no. $\frac{1}{2}$." This sample was used in combination with larger ones to give finer increments in thickness. For example, samples nos. 1 and $\frac{1}{2}$ were used simultaneously to place 6.10 mm of Bi in the beam; we called such a combination "sample no. $1\frac{1}{2}$." The thin sample was also combined with the other samples, to create samples nos. $2\frac{1}{2}$, $3\frac{1}{2}$, and $4\frac{1}{2}$. This doubled the number of data points that could be obtained.

There were 12 data runs taken, using 9 different sample thicknesses. Each run was identified with a sequential run number. There were three early runs, numbers 35, 37, and 38, done with the 8-, 4-, and 12-mm samples, respectively. After a period of computer and apparatus problems, we took a series of 9 more runs, numbered from 73 to 83, using sample thicknesses from 2 to 18 mm, in steps of 2 mm (see Table II). There was a large amount of data generated in these data runs, but we are primarily interested in how the relative contrast in the time slices and in the overall pulse varies as a function of sample thickness D. Table II shows the relative contrast measured in the overall pulse (as in Fig. 8) for all data runs. A plot of the contrast versus D is shown in Fig. 9(a), and is quite similar to the steady-state curves measured in [10] and [11], as one would expect. Note that the contrast falls off rapidly, mainly caused by the wavelength (momentum) spread of the beam [Eqs. (10) and (11)]. The solid line is a predicted curve based on a double Gaussian

TABLE II. Relative contrasts in C3 measured for the overall pulse and for nonoverlapping and overlapping time slices.

Bi sample no.	D (mm)	Relative contrast C_R (percent) Overall pulse	Nonoverlap time slice	Overlap time slice
$\frac{1}{2}$	2.09	84.8±2.4	95.7±8.3	77.3±7.7
1	4.01	55.9±1.9	84.8±6.2	16.5±3.9
		44.1±2.4	80.4±6.2	16.7±4.2
$1\frac{1}{2}$	6.10	11.6±1.3	85.0±7.3	49.8±5.2
2	7.99	14.8±1.5	95.9±8.8	79.2±7.8
		13.1±1.5	73.9±6.7	65.0±6.6
$2\frac{1}{2}$	10.08	8.11±1.59	77.3±7.4	74.8±7.6
3	12.26	2.67±1.47	54.2±6.7	13.7±5.3
		0.93±1.50	48.7±5.3	3.4±4.9
$3\frac{1}{2}$	14.35	4.43±1.64	43.6±6.0	13.9±4.8
4	16.15	3.22±1.62	35.9±5.4	39.5±6.3
$4\frac{1}{2}$	18.24	1.26±1.38	36.5±4.8	38.3±5.5

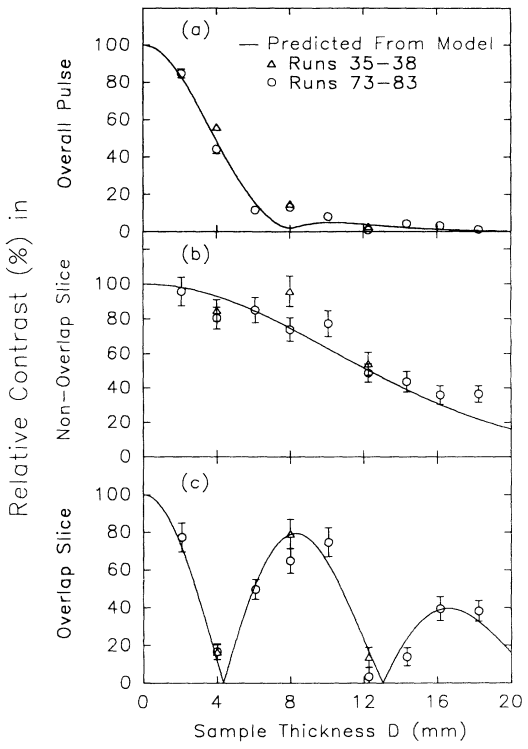

FIG. 9. (a) The relative contrasts in C3 measured in the overall pulse for all data runs, vs the sample thickness D and the predicted curve from a model based on a double Gaussian spectral fit to the actual wavelength distribution. (b) The relative contrasts in C3 measured for all data runs, vs the sample thickness D in the nonoverlap time slice, (c) for the overlap time slice.

spectral fit to the actual wavelength distribution as discussed in [11] and [12].

Of the 11 time slices, we are primarily concerned with the relative contrast results in only two of them. The first is the slice consisting of time channels around 17 and 18 μs (see Fig. 4, left), near the minimum of the pulse intensity. For reasons discussed in Sec. II, this is called the "nonoverlap slice"; it represents the center of each individual pulse, where there is minimal contribution from neighboring pulses. Table II lists also the relative contrast results in the nonoverlap slice for each of the data runs, and Fig. 9(b) shows the data plotted versus D. The solid line is a prediction based on the Gaussian model appropriate for a "nonoverlapping slice" with a narrow wavelength distribution with a width given by Eq. (18). Note that the relative contrast in the nonoverlap slice falls off much more slowly than in the overall pulse [Fig. 9(a)]; there is still contrast in the time slices, even though it seems to have disappeared in the overall pulse.

The second time slice of interest consists of time channels around 7 and 8 μs (see Fig. 4, left), near the maximum of the pulse intensity. This is called the "overlap slice"; as discussed in Sec. II, it is where neighboring pulses most completely overlap. The relative contrast data in the overlap slice are also listed in Table II, for all data runs. Fig. 9(c) shows the contrast plotted versus D; again, the solid line follows from Eq. (24). The resulting curve is much different in the overlap slice than in the nonoverlap slice. The contrast remains high in comparison to the overall pulse [Fig. 9(a)], but it exhibits well-defined oscillations, with minima at $D=4$ and 12 mm, and maxima at $D=0$, 8, and 16 mm. On inspection, the maxima in the overlap slice can be seen to be equivalent to those in the nonoverlap slice, so that Fig. 9(b) seems to define an envelope bounding the contrast oscillations in Fig. 9(c).

IV. DISCUSSION

In this experiment, we were able to carry out a full-scale neutron interferometry experiment in the time domain. The neutron pulses produced by a fast mechanical chopper were significantly shorter than the dimensions of the perfect crystal interferometer, thus assuring that there is no permanent overlap of wave functions or distribution functions at the beam splitting and beam overlapping part of the interference experiment. The experiment again demonstrates very clearly the single-particle interference phenomena in neutron interference experiments because the mean occupation number in a single neutron pulse is much smaller than unity (it is of the order of 10^{-4}). The neutron intensity pulses used in this experiment are considerably longer than the coherence length of the beams and, therefore, diffraction in time effects are negligible. Several aspects of neutron wave mechanics have been explored and have been shown to be in agreement with the theoretical predictions. The spreading of the neutron pulses has been observed as well as the spectral narrowing in distinct time slices downstream from the interferometer.

The excellent agreement between the predicted contrast curves and the measured data, particularly in Fig. 9, shows that our model correctly describes the propagation of neutron pulses, the separation of the wavelength components, as well as the various corrections necessary to extract the experimental results. In Sec. II the formulas for single Gaussian distributions are given although the detailed data evaluation has included the double Gaussian nature of the actual wavelength spectra [22]. As in our other recent papers [10–12], we have found a way to extract interference fringes (i.e., contrast) from a beam which, on the whole, exhibits no contrast. Thus, an interference and coherence phenomena can be completely hidden due to general averaging effects but it can be recovered even behind the interferometer if a proper measuring procedure is applied.

The observed beam modulation occuring in the overlap region of successive pulses is another example how intrinsic coherence phenomena become manifest. In this case when time resolution is applied the average intensity remains constant—aside from attenuation effects—but

the contrast shows a marked beat effect. This behavior is characteristic for the incoherent beam superposition of two different wavelength bands.

Furthermore, it is our hope that our time-dependent neutron interferometry effects, such as quantum chopping (phasing) or Miller-Wheeler delayed choice experiments [23] will soon be investigated.

ACKNOWLEDGMENTS

This work was supported by the Physics Division of the NSF (Grants Nos. PHY-8813253 and PHY-9024608), the U.S.-Austria program at NSF (Grant No. INT-8712122), and Fonds zur Förderung der Wissenschaftlichen Forschung (Project No. S4201) in Austria.

---

*Present address: VÖEST-Alpine AG, A-4020 Linz, Austria.

†Present address: Physics Department, Bethany College, Bethany, WV 26032.

[1] *Neutron Interferometry,* edited by U. Bonse and H. Rauch (Clarendon, Oxford, 1979).

[2] A. G. Klein and S. A. Werner, Rep. Prog. Phys. **46**, 259 (1983).

[3] *Matter Wave Interferometry,* edited by G. Badurek, H. Rauch, and A. Zeilinger (North-Holland, Amsterdam, 1988).

[4] M. Born and E. Wolf, *Principles of Optics* (Pergamon, Oxford, 1975).

[5] D. Petrascheck, Phys. Rev. B **35**, 6549 (1987).

[6] A. Stern, Y. Aharonov, and Y. Imry, Phys. Rev. A **41**, 3436 (1990).

[7] H. Rauch, in *Neutron Interferometry* (Ref. [1]), p. 161.

[8] H. Kaiser, S. A. Werner, and E. A. George, Phys. Rev. Lett. **50**, 563 (1983).

[9] H. Rauch, E. Seidl, D. Tuppinger, D. Petrascheck, and R. Scherm, Z. Phys. B **69**, 313 (1987).

[10] R. Clothier, H. Kaiser, S. A. Werner, H. Rauch, and H. Wölwitsch, Phys. Rev. A **44**, 5357 (1991).

[11] H. Kaiser, R. Clothier, S. A. Werner, H. Rauch, and H. Wölwitsch, Phys. Rev. A **45**, 31 (1992).

[12] S. A. Werner, R. Clothier, H. Kaiser, H. Rauch, and H. Wölwitsch, Phys. Rev. Lett. **67**, 683 (1991).

[13] J. Summhammer, H. Rauch, and D. Tuppinger, Phys. Rev. A **36**, 4447 (1987).

[14] H. Rauch and J. Summhammer (unpublished).

[15] H. Wölwitsch, Ph.D. thesis, Technical University of Vienna, 1988.

[16] M. Heinrich, H. Rauch, and H. Wölwitsch, Physica **156&157B**, 588 (1989).

[17] J. Kulda, P. Lukas, P. Mikula, Y. A. Alexandrov, L. N. Sedlakova, M. Vrana, and H. Rauch, Nucl. Instrum. Methods A **300**, 80 (1991).

[18] A. Messiah, *Quantum Mechanics* (North-Holland, Amsterdam, 1965).

[19] M. Moshinsky, Phys. Rev. **88**, 625 (1952).

[20] R. Gähler and R. Golub, Z. Phys. B **56**, 5 (1984).

[21] V. G. Nosov and A. I. Frank, J. Moscow Phys. Soc. **1**, 1 (1991).

[22] R. Clothier, Ph.D. thesis, University of Missouri–Columbia, 1991.

[23] W. A. Miller and J. A. Wheeler, in *Proceedings of the International Symposium on the Foundations of Quantum Mechanics,* edited by H. Ezawa *et al.* (Physical Society of Japan, Tokyo, 1983), p. 38.

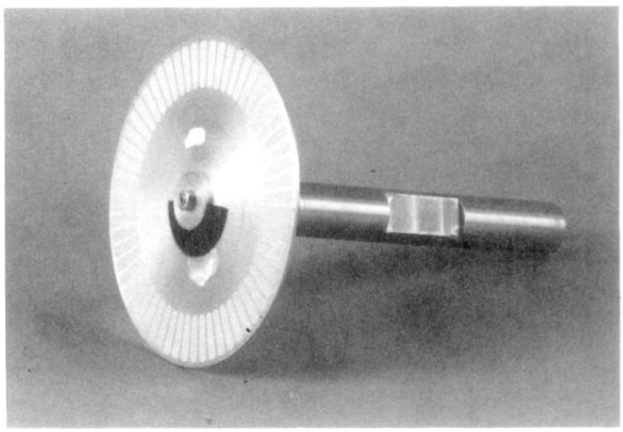

FIG. 2. Photograph of the neutron chopper disk showing also the magnetized shaft for the magnetic bearing.